energies

Article

Optical and Thermal Performance of Linear Fresnel Reflectors in Eastern Mediterranean Conditions

Dimitrios Graikos [1,2], Lazaros Aresti [1,2], George Constandinides [2,3], Savvas Tassou [4], Toula Onoufriou [2,3] and Paul Christodoulides [1,*]

[1] Faculty of Engineering, Cyprus University of Technology, 3036 Limassol, Cyprus; dimitrios.graikos@cut.ac.cy (D.G.); lg.aresti@edu.cut.ac.cy (L.A.)
[2] EMERGE CoE, 3036 Limassol, Cyprus; g.constandinides@cut.ac.cy (G.C.); t.onoufriou@cut.ac.cy (T.O.)
[3] Department of Civil Engineering and Geomatics, Cyprus University of Technology, 3036 Limassol, Cyprus
[4] Centre for Sustainable Energy Use in Food Chain (CSEF), Department of Mechanical and Aerospace Engineering, Brunel University London, Uxbridge UB8 3PH, UK; savvas.tassou@brunel.ac.uk
* Correspondence: paul.christodoulides@cut.ac.cy

Abstract

Linear Fresnel Reflectors (LFR) are a type of concentrated solar collector that uses direct solar radiation (DSR) to provide useful heat for a range of applications, including power generation, heating and cooling. This study introduces a simplified analytical method for predicting the optical and thermal performance of LFR systems using only the geometric parameters and meteorological data of a location. In this analysis, the Incident Angle Modifier (IAM) and DSR are calculated using long-term data from open-access weather datasets, offering analysis from minute-scale to annual resolution, without the requirement of computationally expensive methods such as ray-tracing or extensive onsite measurements. The model is validated against experimental data from an installed LFR system at the Cyprus Institute (CyI) in Nicosia, Cyprus, demonstrating good agreement in both solar and useful energy output. The latter is derived as the product of the predicted DSR, which closely matches pyrheliometer measurements over a four-year period, and the accurately reproduced IAM. Overall, the method provides a reliable estimation of the thermal performance, offering a practical tool for early-stage design for any location of interest, yielding results significantly faster and at a fraction of the computational cost compared to ray-tracing and CFD approaches.

Keywords: solar energy; solar collector; linear fresnel collector; optical efficiency; thermal efficiency; direct solar radiation; 1D modeling

Check for updates

Academic Editor: Armando Oliveira

Received: 13 June 2026
Revised: 4 July 2026
Accepted: 24 July 2026
Published: 5 August 2026

1. Introduction

The continuous increase in energy demand, the depletion of fossil fuel reserves, and green policies against climate change have prompted engineers to invest in renewable energy sources, with solar energy being one of the most promising solutions for electricity production in the form of photovoltaic panels or for thermal energy via solar energy collectors.

Solar collectors can be divided into two main categories: 'non-concentrating', which are usually stationary, and 'concentrating', which provide a larger ratio of aperture-to-absorber area and are capable of high temperatures and are ideal for power generation [1,2]. Concentrated solar power (CSP) facilities could produce solar-only or solar-enhanced fuels by 2030 and, by 2050, produce enough hydrogen to replace 3% of the global natural gas consumption and up to 3% of liquid fuels [3]. CSP systems can store solar radiation in the form of heat, which is a significantly cheaper and simpler method than reserving energy in batteries in PV systems [4,5].

Regarding concentrating solar collectors, several types are commonly used, including (i) Parabolic Trough Collectors (PTC), (ii) Fresnel Collectors, (iii) Solar Tower and (iv) Parabolic Dish Reflectors. Each type can be further classified depending on how solar radiation is focused on the receiver [6,7].

With respect to Fresnel collectors, there are two types: the Fresnel Lens Collectors and Linear Fresnel Reflectors (LFR). The latter type and its characteristics form the object of the present study. In LFRs, an array of linear mirror strips is used to reflect the incident solar radiation onto a linear receiver. This enables LFRs to reach medium-to-high temperatures, typically operating at 250–390 °C, with concentration ratios of up to 80 when secondary reflectors are included in large-scale installations [6,8,9]. The mirror strips can be either flat or slightly curved and are mounted on a flat surface or the ground. Flat mirrors offer simplicity but limited concentration capability, while curved geometries, including parabolic or cylindrical profiles, provide improved flux distribution at the receiver. Pulido-Iparraguirre et al. [10] demonstrated that even small deviations in mirror curvature or facet assembly can noticeably alter the reflected solar radiation, highlighting the importance of accurate mirror shaping in LFR performance. The mirrors track the sun along a single axis throughout the day, typically rotating in the east–west direction for operational convenience. The working fluid of LFR systems may include water or superheated steam at high pressures that can be used directly in a turbine for power generation. Oils and molten salts can be used to achieve temperatures up to 400 °C and 560 °C, respectively [11–15]. Examples of LFRs have been reported with annual electrical efficiency of 9.3% for the region of Dagget, CA (USA) [16], and 10.9% for Athens, Greece [17]. In the latter case, a mean incident angle modifier (IAM) of 58.7% was reported, with the cost of the LFR system reaching 185 €/m^2, yielding an 8- to 9-year payback period of investment.

López-Núñez et al. [18] assessed the energy generation of an LFR prototype in Morelos, Mexico through a finite-volume model in ANSYS Fluent R16. Comparing their results with experimental data [19] yielded a maximum relative error of 2.36% for a 28% energy efficiency. Concentrating solar technologies can also be combined with PV panels; Çalık and Fırat [20] reported a photovoltaic thermal efficiency of 15.8% for a PV system coupled with flat mirrors with no blocking and shading, using solar data for a case study in Istanbul, Turkey. Wang et al. [21] reported experimentally validated efficiencies of 14.7% and 13.6% for the solar cell monomer and module, respectively, which were both higher than 12.3% and 10.7% for a PTC in China. Machado et al. [22] have modeled several photovoltaic (CPV) systems, including LFRs, using the Monte Carlo ray-tracing method and shown that reflector misalignment and other optical errors can significantly reduce the amount of solar radiation reaching the receiver, highlighting the sensitivity of LFR performance to geometric parameters.

Calculating the optical and thermal efficiency of an LFR can prove challenging due to the large number of mirrors that rotate independently. Geometry is required to determine the mirror angles, concentration ratio and IAM. Despite significant progress, many existing approaches rely on detailed ray-tracing or site-specific experimental and CFD-based calibration [18,19,21,23]. While such methods provide high accuracy, they are computationally demanding and require detailed geometric or experimental inputs and are, therefore, less suitable for early-stage design and rapid assessments. These limitations reduce their transferability to new sites, particularly where long-term measurements are unavailable. Simplified analytical models based on geometric incident angle modifiers (IAMs) have been proposed as an alternative by Bellos et al. [24]. However, they often assume idealized

https://doi.org/10.3390/en19153686

mirror configurations. Rungasamy et al. [23] performed a comprehensive review on LFR optical design, providing analytical, ray-traced and CFD results. Other indicative studies featuring numerical and CFD methods were presented by Nunez et al. [18,19].

Grena [25] has conducted a comprehensive review of the geometrical aspects of LFR optics, showing that shadowing, blocking and positioning of the mirrors significantly affect the optical efficiency. Detailed ray-tracing methods can be used to capture these effects. However, the author argues that such methods are computationally intense and often unnecessary for performance prediction. This highlights the need for simplified tools.

In addition, the adoption of LFR systems in industrial applications not related to power generation often lacks simple tools to evaluate whether such systems can be integrated for their purposes. Sepúlveda et al. [26] provided an extensive analysis of the potential use of such systems in the food and sanitary industry and showed that many facilities lack straightforward methods to determine the suitability of CSP technologies based on their specific energy requirements.

Mahmood and Hossin [12] presented a theoretical analysis of the daily, monthly and annual thermal performance of an LFR system, which was coupled with an organic Rankine cycle and a two-tank thermal storage unit. The DSR was obtained from the typical meteorological year (TMY), which provided the hourly irradiance values over a full year for the region of Almatret, Spain. The thermal analysis was carried out for selected representative days in each month and then used to infer the monthly and annual performance. The IAM was determined using polynomial curve fit coefficients derived from Monte Carlo ray-tracing simulations, which required the exact geometry of the system. The thermal performance of the receiver was then evaluated through detailed heat transfer equations accounting for convective and radiative losses, and the results were propagated through the full ORC and thermal storage subsystems.

Bellos et al. [27] conducted a similar study for the climate conditions of Athens, Greece. The direct solar radiation (DSR) was derived from the ASHRAE model [28], with the empirical parameters taken from the literature. The IAM in both the longitudinal and transversal directions was obtained from CFD simulations, producing polynomial curve fit expressions as functions of the incident angle. The curves were inserted into a dynamic numerical model that solved the storage tank energy balance at 30 s time steps for twelve representative days, one per month, with the yearly performance inferred from the results of these selected days weighted by the number of sunny days per month. While this approach provides a detailed energetic and exergetic characterization of the system, it requires dedicated CFD software, a fully resolved 3D collector geometry, and significant computational effort for the optical simulations prior to the dynamic analysis.

Boccalatte et al. [29] proposed an IAM correlation based on solar declination and zenith angles. The constants involved were calculated through a regression analysis on year-round 3D, hourly ray-tracing simulations of given LFR geometries. The authors reported that such analysis produces large datasets that require significant computational effort, and that the regression coefficients are geometry-specific and must be derived again for each new configuration through a dedicated ray-tracing campaign, making such an approach computationally expensive and challenging to process.

Experimental characterization of LFR systems presents significant practical challenges. Sallaberry and Mutuberrial [30] reported that determining the optical efficiency and IAM of a large-scale LFR system through onsite testing required measurements over the span of nine months. This included calibrated instrumentation combined with ray-tracing simulations to compensate for incident angles that were unachievable due to the geographical location of the installation. Such an approach is unsuitable for parametric studies or early-stage design evaluation, where rapid and low-cost performance estimates are required.

https://doi.org/10.3390/en19153686

The aim of this study is to present a simple, fast and inexpensive method for predicting the optical and thermal performance of an LFR system using only its geometric parameters and open-access meteorological data. The relevant geometric characteristics provide the necessary optical performance (i.e., the IAM), while using the meteorological data enables the determination of direct solar radiation (DSR) throughout the year. This allows the analysis to be carried out from minute-scale resolution to annual performance without the need for complex, computationally expensive ray-tracing tools, CFD, or extensive on-site measurements prior to installation. The method is then validated against experimental data from an installed LFR system at the Cyprus Institute, Nicosia, Cyprus [31], allowing for a direct comparison of the thermal results.

Ultimately, the current study offers a 1D tool for rapid thermal performance estimation at any location. The novelty of the present work lies in the development of a low-cost modeling framework that combines simplified geometric parameters with long-term open-access meteorological data to predict the thermal performance of LFR systems. The present approach couples two optical and solar radiation models into a simple method that eliminates the need for on-site instrumentation during the preliminary design phase, relying on available weather data and desired design parameters, while offering a high-resolution analysis spanning from minute to annual timescales. Compared to ray-tracing or CFD-based approaches, which typically require exact geometry, specialized software, and significant setup time, with individual simulations taking hours to days, the present method operates with only basic geometric inputs and produces equivalent annual performance estimates within seconds, representing a reduction in computational effort of several orders of magnitude. This assists with the decision-making on whether such a system is fit for purpose at a chosen site.

2. Problem Formulation

The weather data for the region of Nicosia were obtained from the PVGIS-SARAH3 tool [32] and are used to derive the DSR and temperature variation. The results are then compared with measured data from a pyrheliometer. Optical, solar, and thermal analyses are conducted to evaluate the performance of the LFR system ranging from an hourly to an annual basis, and the results are compared with the corresponding measured data.

2.1. LFR Optical Analysis

The optical efficiency η_{opt} is defined as the ratio of the energy absorbed by the absorber to the total incident solar energy on the collector's aperture; it is calculated as the product of various unitless parameters [1]:

$$\eta_{opt} = \alpha \cdot \gamma \cdot \rho \cdot \tau \cdot K = \eta_{opt,max} \cdot K \tag{1}$$

where a is the absorbance of the absorber, γ is the intercept factor, ρ is the reflectance of the reflector, τ is the transmittance of the cover, and $\eta_{opt,max}$ is the maximum optical efficiency, given as the product of these parameters, which are typically provided by the manufacturer. In addition, K is the IAM, which varies throughout the day, as it is directly influenced by the solar incident angle θ. The latter can be analyzed in two directions, namely the longitudinal incident solar angle (θ_L) and the transversal incident angle (θ_T), as shown in Figure 1. Clearly, the maximum optical efficiency $\eta_{opt,max}$ is achieved when K = 1, corresponding to $\theta_L = \theta_T = 0$. Therefore, the IAM can be expressed as the ratio of the optical efficiency to the maximum optical efficiency [24]:

$$K(\theta_L, \theta_T) = \frac{\eta_{opt}(\theta_L, \theta_T)}{\eta_{opt,max}} \tag{2}$$

or approximated as the product of its longitudinal and transversal components [33]:

$$K \approx K_L(\theta_L) \cdot K_T(\theta_T) \tag{3}$$

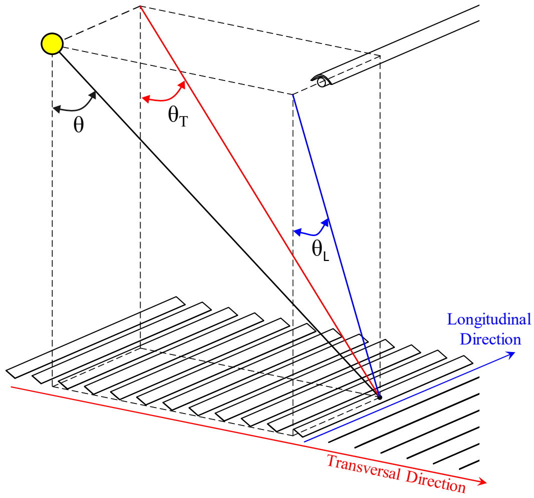

Figure 1. Solar incident angles along the transversal and longitudinal direction.

Bellos and Tzivanidis [24] proposed analytical equations for each IAM component as functions of the geometric parameters of the LFR, and the key dimensions are illustrated in Figure 4.

The IAM in the longitudinal direction K_L is calculated as:

$$K_L(\theta_L) = \cos(\theta_L) - \frac{F}{L_c} \cdot \sin(\theta_L) \cdot \sqrt{1 + \left(\frac{W}{4F}\right)^2} \tag{4}$$

where F is the focal distance, F_i is the distance of each mirror from the absorber, L_C is the collector length, W is the width between the centers of the first and last mirror, W_0 is the mirror width, and D_w is the distance between reflectors (all in m).

While in the transversal direction, for $K_{T,}$ there are two cases that depend on the critical angle θ_{crit}: for $\theta_T < \theta_{T,crit}$,

$$K_T(\theta_T) = \cos\left(\frac{\theta_T}{2}\right) - \frac{W/4}{F + \sqrt{F^2 + (W/4)^2}} \cdot \sin\left(\frac{\theta_T}{2}\right) \tag{5}$$

and for $\theta_T \geq \theta_{T,crit}$,

$$K_T(\theta_T) = \left[\cos\left(\frac{\theta_T}{2}\right) - \frac{W/4}{F + \sqrt{F^2 + (W/4)^2}} \cdot \sin\left(\frac{\theta_T}{2}\right)\right] \cdot \left[\frac{D_w}{W_0} \cdot \frac{\cos(\theta_T)}{\cos\left(\frac{\theta_T + \varphi_m}{2}\right)}\right] \tag{6}$$

The critical transversal angle $\theta_{T,crit}$ is used to account for the shading effects/optical losses that occur between the adjacent mirror strips. For small transversal angles (up to 30°), shading does not occur. However, at larger angles, the shading effects become significant. The critical angle can be calculated as:

$$\cos(\theta_{T,crit}) = \frac{W_0}{D_w} \cdot \cos\left(\frac{\theta_{T,crit} + \varphi_m}{2}\right) \tag{7}$$

The mean position angle of the mirror φ_m is calculated using the geometry shown in Figure 4:

$$\varphi_m = 2 \cdot \arctan\left[\frac{W/4}{F + \sqrt{F^2 + (W/4)^2}}\right] \quad (8)$$

Although the equations above offer a convenient way to calculate the IAM, the model was developed for flat primary mirrors that are separated by constant gaps, while the efficiency of the secondary reflector and any blocking or shading effects associated with it are not taken into account.

The LFR system under consideration from The CyI is shown in Figures 2 and 3. It was designed by IDEA srl [31] and has supplied heating and cooling to the building described by Montenon et al. [34] and Papanicolas et al. [35]. The system operates in the medium-temperature range and employs a receiver composed of eight evacuated tubes connected in series, with each 4 m long. These tubes are coupled with a parabolic secondary reflector positioned above them to enhance the optical concentration. The primary concentrator consists of 18 rows of rectangular and slightly curved mirrors. Each row contains 8 mirrors, each with dimensions 4 m × 0.32 m, giving a reflective area of 10.24 m^2 per row. The spacing between rows is variable, with an average separation of 0.43 m. The total width of the field from the first to the last row is 7.8 m, while the collector length is 32.5 m. The optical design has a focal distance of 3.6 m. The geometric characteristics of the LFR are summarized in Table 1, and they are also illustrated graphically in Figure 4.

Table 1. Geometric characteristics of LFR collectors selected from the literature.

Collector Type	Collector Geometry					
	W (m)	F (m)	L_C (m)	W_0 (m)	D_w (m)	θ_{crit} (°)
Bellos et al. [24]	6	3	6	0.15	0.2	56
The CyI [31]	7.8	3.6	32.5	0.32	0.433	57

The incidence angle modifier is calculated using the analytical expressions presented in Section 3. Specifically, K is calculated as the product of K_L and K_T, as described in Equations (4)–(6) depending on the critical angle. Although the geometric characteristics of the CyI collector differ from those of the Bellos, the resulting values of $\theta_{T,crit}$ are nearly identical, indicating that both collectors exhibit similar shading. Figure 5 presents the measured and predicted values of the incidence angle modifier K as a function of the incident angle θ for both the CyI LFR system and the collector analyzed by Bellos et al. [36], using the geometric characteristics listed in Table 1. The experimental data are shown with circles and triangles, while the continuous lines correspond to the model predictions. Both collectors exhibit the expected monotonic decrease of K with increasing θ, but with different slopes. The model accurately reproduces the IAM behavior of the Bellos collector, which employs flat primary mirrors with uniform spacing, resulting in perfect collapse between the data and the model.

On the other hand, the model CyI overestimates K across the full angular range, with all predicted values lying above the measured data. This is attributed to the non-uniform spacing and the assumption of an average D_w. This is in agreement with Grena's [25] observation that non-uniform mirror spacing can significantly affect the optical behavior of an LFR, particularly the onset of blocking and shading at large transversal angles. Additionally, the CyI primary mirrors are slightly curved, whereas the model assumes flat mirrors. This curvature affects the reflected flux distribution and concentration at the receiver, contributing further to the discrepancy.

However, the model correctly reproduces the shape of K, while the predicted magnitudes are considered adequate to characterize the optical behavior of the system, given the simplicity of the geometric inputs. To quantify the agreement, an error analysis was performed over the range of 0–70°, since for angles above that value, the K approaches zero, which could inflate the MAPE artificially. The analysis showed an RMSE of 0.051, a MAPE of 23%, and an R^2 of 0.975. The high R^2 confirms that the trend is well-captured, while the MAPE reflects the systematic overestimation as a consequence of the geometric simplifications.

The effect of uniform mirror spacing D_w on the IAM prediction has been studied through a sensitivity analysis, with the full results presented in Appendix A.1. The analysis was conducted by systematically varying D_w (while maintaining the constant spacing between the rows) from its physical lower limit, imposed by the mirror width W_0, below which θ_{crit} becomes undefined, up to double the baseline value. The results are graphically presented in Figure A1, demonstrating that reducing the mirror spacing below the baseline consistently improves agreement with the measured CyI data across all error metrics, with the best case (D_w = 0.320 m, −26% from baseline) yielding an RMSE of 0.027, a MAPE of 10%, and an R^2 of 0.993. Conversely, increasing D_w worsens the predictions up to a plateau at +50% (D_w = 0.65 m), beyond which any further increase has no additional effect, as clearly shown in Figure A2. Importantly, the analysis also revealed that, at low incidence angles ($\theta < 30°$), all D_w cases converge regardless of spacing, indicating that mirror curvature, rather than spacing, is a dominant source of error in this regime. However, the effect of mirror curvature cannot be evaluated within the current form of analytical equations, as these were derived under the assumption of flat primary mirrors. These two error sources are, therefore, independent and would need to be addressed separately to achieve a full correction.

For LFR configurations with strongly non-uniform mirror spacing or significantly curved primary mirrors, the present model should be applied with caution. In such cases, the IAM prediction will represent an upper bound, and the magnitude of overestimation will scale with the degree of geometric deviation from the idealized assumptions.

Figure 2. The LFR system under consideration located in Nicosia, Cyprus [37].

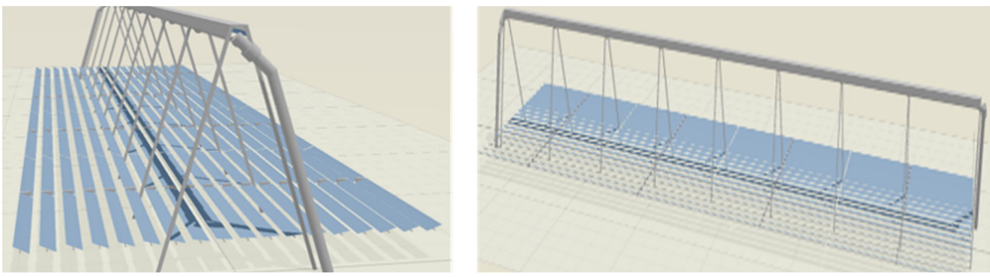

Figure 3. CAD representation of the LFR system adapted from Tonatiuhpp [38].

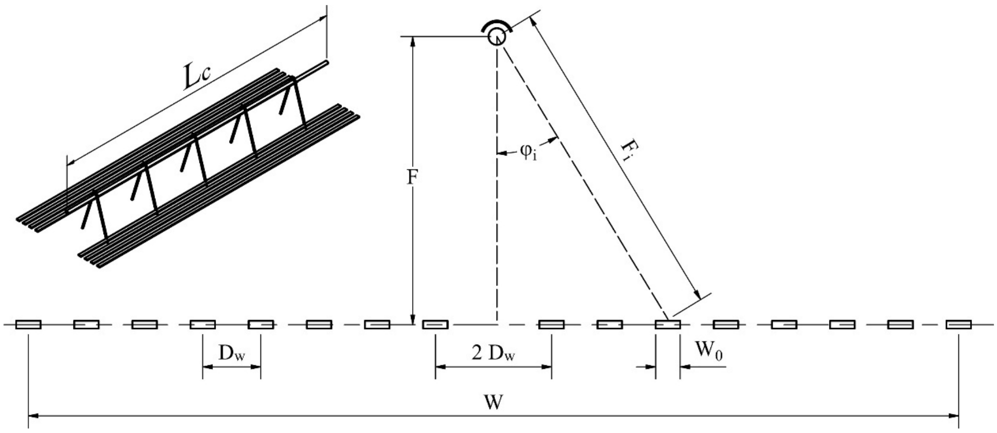

Figure 4. Simplified model of an LFR system with required dimensions.

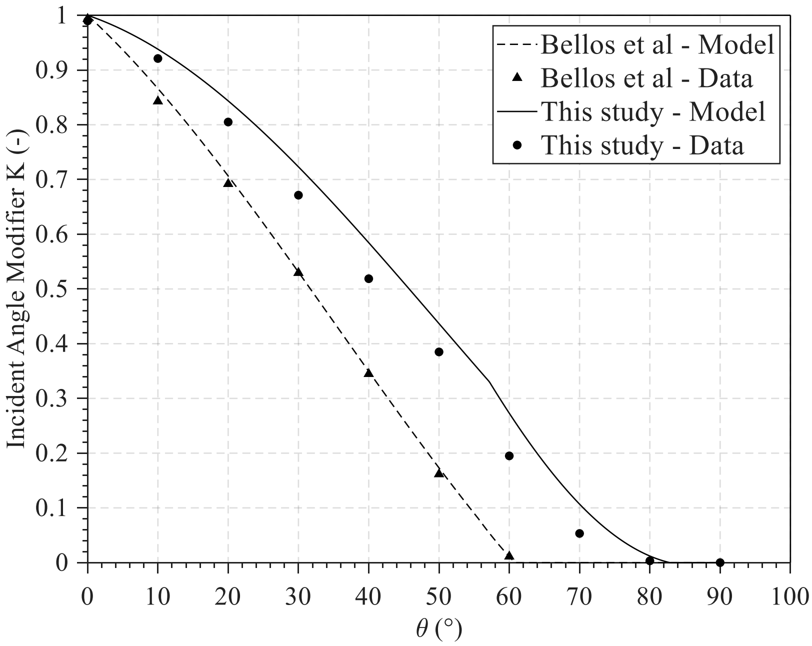

Figure 5. Incident angle modifier for selected LFR collectors from the literature. (Continuous and dashed line—model, filled circles and triangles—collector data) [24]. Error metric for this study: RMSE = 0.051, MAPE = 23% and R^2 = 0.975.

2.2. Solar Analysis

The basic solar angles describing the position of the sun are shown in Figure 6. Although the following equations represent standard solar geometry relations widely used in the literature [1], they are presented here to aid the reader and to establish a connection between the optical analysis of Section 2.1 and the solar model of Section 2.3. Specifically, the longitudinal and transversal incidence angles, θ_L and θ_T, used in the IAM calculations of Equations (4)–(8), are derived from the solar altitude, zenith, and azimuth angles presented in this section. The solar declination angle δ is calculated as a function of the day number N (=1, 2, . . . , 365):

$$\delta = 23.45 \cdot \sin\left[\frac{360}{365}(284 + N)\right] \tag{9}$$

The hour angle (h) is calculated as:

$$h = (t_{AST} - 12) \cdot 15^{\circ} \tag{10}$$

where t_{AST} is the apparent solar time (measured in hours). The solar altitude (α) and zenith angle (Φ) are complementary angles:

$$\Phi + \alpha = 90^\circ \tag{11}$$

and

$$\sin(a) = \cos(\Phi) = \sin(L)\cdot\sin(\delta) + \cos(L)\cdot\sin(\delta)\cdot\cos(h) \tag{12}$$

where L is the local latitude. Finally, the solar azimuth angle z is given by:

$$\sin(z) = \frac{\cos(\delta)\cdot\sin(h)}{\cos(a)} \tag{13}$$

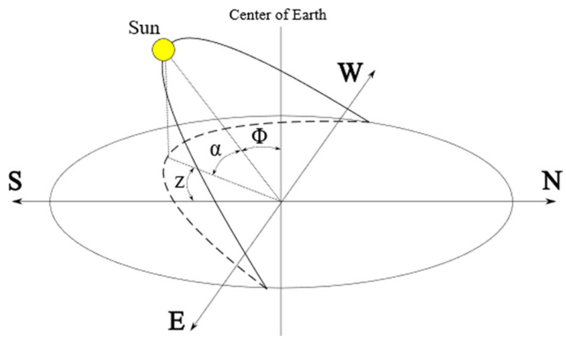

Figure 6. Apparent daily path of the sun across the sky with the most important solar angles.

The longitudinal and transversal angles are calculated by projecting the incident solar angle components in each direction (see Figure 1).

$$tan(\theta_L) = cos(z)\cdot tan(\Phi) = \cos(z)\ /\tan(a) \tag{14}$$

and

$$tan(\theta_T) = sin(z)\cdot tan(\Phi) = \sin(z)\ /\tan(a) \tag{15}$$

2.3. Weather Data and Direct Solar Radiation

Several empirical models for estimating the components of solar radiation have been proposed in the literature [39–41], and their main characteristics are summarized in Table 2. In this study, the empirical model originally developed by ASHRAE [28] and later applied by Kouremenos et al. [42] is adopted for calculating the DSR as expressed in Equation (16), where G_b is the DSR. The ASHRAE empirical model was selected for three reasons. First, it requires only two site-specific empirical parameters (A and B) that can be calibrated using long-term averaged open-access data without the need for radiosonde profiles, aerosol optical depth profiles, or precipitable water content measurements. Second, the semi-arid Eastern Mediterranean climate of Cyprus is characterized by predominantly clear-sky conditions, under which the ASHRAE formulation yields reliable results. Third, the primary objective of this work is to provide a preliminary design tool; more advanced transmittance models (e.g., Bird–Hulstrom, Linke turbidity-based approaches) typically require specific inputs that may be unavailable at the early design stage or accessible only through paid datasets.

Application of this model requires long-term weather data for the local region (generally 12 years or more [42]) to determine the apparent solar radiation at zero air mass, A (W m^{-2}), and the atmospheric extinction coefficient, B (unitless). It should be noted that Equation (16) represents a simplified form of the original empirical expression, which also includes a diffuse radiation factor, C (unitless), used for estimating the global solar radiation on a horizontal surface. This component lies outside the scope of the present work. The daily variations of parameters A and B for the region of Nicosia were derived using averaged open-access meteorological data from PVGIS [32] over a 19-year period (2005–2023) and are illustrated in Figure 7.

$$G_b = A \cdot \exp\left[-\frac{B}{\sin(a)}\right] \tag{16}$$

Table 2. Characteristics of selected radiation models.

Model	Type	Characteristics
Ghouard (1977) [41]	Empirical	Disturbing factor evaluations depending on the atmospheric conditions and astronomical parameters. i.e., turbidity factors
Perrin Brichambaut [43]	Empirical	Based on astronomical parameters and empirical constants A, B, C; estimates direct, diffuse, and global radiation. Good performance under clear skies; easy to implement.
Capderou [44]	Semi-empirical	Uses the Linke turbidity factor to calculate the direct and diffuse solar radiation components received on horizontal plane.
Bird and Hulstrom [45]	Semi-empirical	Includes the function of absorption and transmittance by the atmospheric components such as ozone, gas, water and aerosols
ASHRAE (Kouremenos) [42]	Empirical	Empirical constants A, B, C; estimates direct, diffuse, and global radiation. Can be used with long time-averaged data.

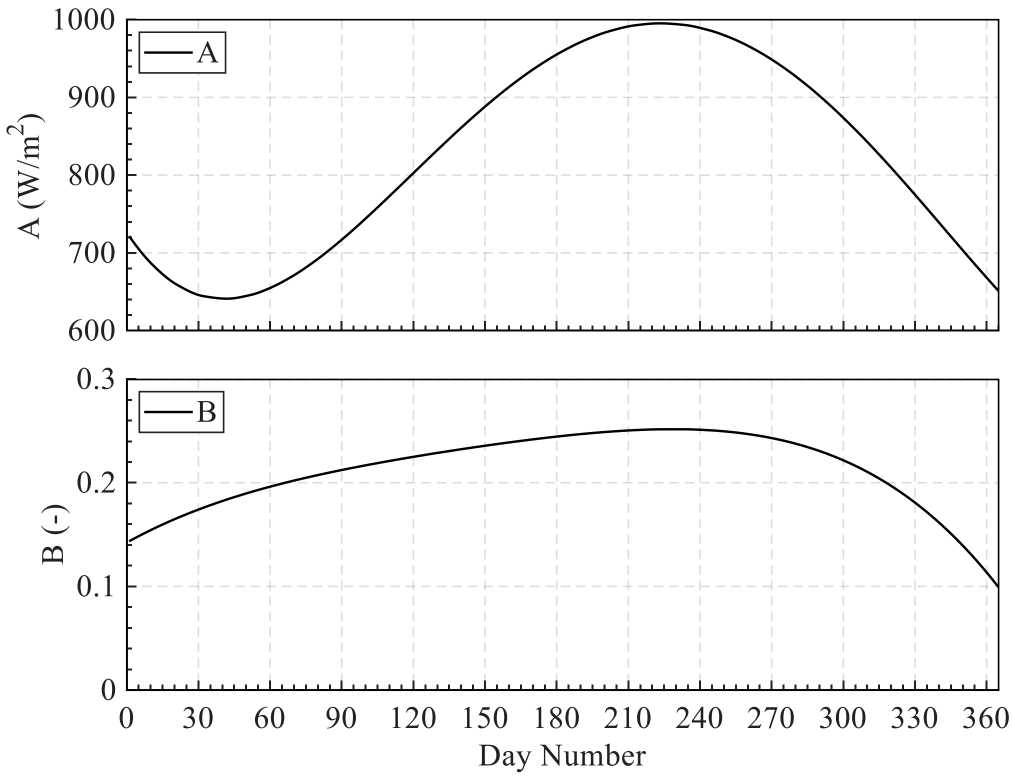

Figure 7. Coefficients A and B for the case study in Nicosia.

The sensitivity of the calibrated parameters A and B can be assessed depending on the selected length of the meteorological data. For that reason, the dataset was split into two overlapping 13-year subperiods (2005–2017 and 2011–2023), and the A and B coefficients were derived independently for each, as shown in Figure A3 in Appendix A.2. The maximum deviations from the full 19-year period were also summarized in Table A1. The deviations are evaluated relative to the full 19-year period, with the largest deviations for A and B being 11% and 15%, respectively. These maximum values occur in late December, when solar angles are at their lowest and clear-sky days are least frequent. Overall, the 19-year dataset provides a more representative calibration than either subperiod alone.

The efficiency of a solar collector is affected by the ambient temperature T_{am}, which is usually assumed to maximize at 14:00 and can be expressed as:

$$T_{am} = T_{am,m} + \frac{DR}{2} \cdot \cos\left(2\pi \frac{t_{AST} - 14}{24}\right) \quad (17)$$

where $T_{am,m}$ is the average daily temperature (in °C), and DR is the daily temperature variation (in °C).

2.4. Thermal Analysis

The energy output and performance of the system are determined through the thermal analysis of the collector. The useful heat $\dot{Q}_u$ is defined as the temperature rise of the working fluid inside the collector and is given by:

$$\dot{Q}_u = \dot{m} \cdot C_p \cdot (T_{out} - T_i) \quad (18)$$

where $\dot{m}$ is the mass flow rate of the working fluid (in kg s^{-1}), C_p is the specific heat capacity of the working fluid (Oil: 2360 J kg^{-1} K^{-1}), T_i is the inlet temperature of fluid (in °C) and T_{out} is the outlet temperature of fluid (in °C). The amount of the DSR G_b that is collected over the aperture area, A_a (in m^2), of the collector results in the incident solar radiation $\dot{Q}_s$ calculated as follows:

$$\dot{Q}_s = A_a \cdot G_b \quad (19)$$

while the thermal efficiency is defined as the ratio of the delivered useful heat $\dot{Q}_u$ to the incident solar radiation $\dot{Q}_s$, i.e.,

$$\dot{Q}_u = \eta_{th} \cdot \dot{Q}_s \quad (20)$$

where manufacturers of solar collectors usually express the thermal efficiency η_{th} as a function of the working fluid inlet temperature, the ambient temperature, the direct solar radiation, and the IAM, which for the LFR system under consideration is given as:

$$\eta_{th} = 0.464K - 0.0657 \cdot \frac{T_i - T_{am}}{G_b} - 0.0002 \cdot \frac{(T_i - T_{am})^2}{G_b} \quad (21)$$

Note that the empirical coefficients in Equation (21) apply strictly for the system under consideration. Additionally, here it is assumed that T_i = 100 °C. Finally, the mean IAM, $\overline{K}$, for a time period, is given by:

$$\overline{K} = \frac{\int_{t_1}^{t_2} K \cdot G_b \, dt}{\int_{t_1}^{t_2} G_b \, dt} \quad (22)$$

The solar (E_s) and useful energy (E_u) over a time period are calculated as:

$$E_s = \int_{t_1}^{t_2} \dot{Q}_s dt \quad (23)$$

and

$$E_u = \int_{t_1}^{t_2} \dot{Q}_u dt \quad (24)$$

The key assumptions for the optical and radiation model are stated once again for clarity. These include (i) flat primary mirrors with uniform spacing (average D_w used for the CyI system), (ii) secondary reflector losses and mirror curvature effects are neglected, (iii) clear-sky conditions are assumed, (iv) the thermal efficiency coefficients are as supplied by the manufacturer and are treated as fixed, and (v) a steady-state thermal model is used, neglecting transient effects such as thermal inertia and start-up losses.

The analysis presented in Section 2 can be summarized in the Figure 8.

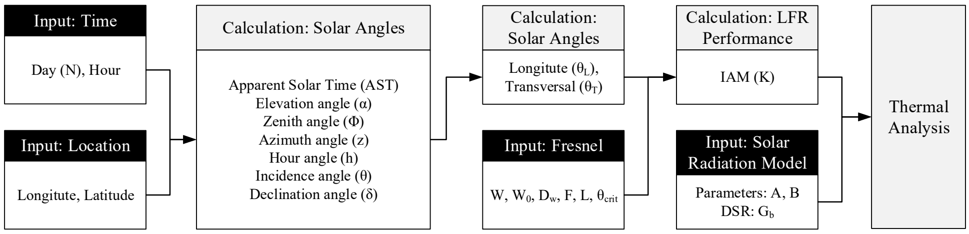

Figure 8. Flow chart for calculation of thermal performance.

3. Results and Discussion

The mathematical framework presented in the previous sections and summarized in Figure 8 enables the performance of the Linear Fresnel Reflector system to be evaluated over different time scales ranging from hourly operation to long-term annual performance. In this section, the predicted results are analyzed and compared with the experimental measurements obtained from the LFR installation at the Cyprus Institute in Nicosia, Cyprus, including solar data from a pyrheliometer.

3.1. Solar Radiation Model Validation

Direct Solar Radiation (DSR) represents one of the most influential parameters affecting the performance of concentrating solar collectors, as only the direct component of solar radiation can be effectively concentrated by reflective optics. Figure 9 shows the hourly profile of G_b over the span of a day, for the winter and summer solstices (21 December and 21 June, respectively). The dashed and continuous lines represent the predicted DSR, while the closed circles and triangles correspond to the 19-year averaged open-access data from PVGIS [32]. The results demonstrated good agreement. For the summer solstice, the model achieves an RMSE of 37 W/m^2, a MAPE of 7%, and an R^2 of 0.96, while for the winter solstice, the corresponding values are 45 W/m^2, 8%, and 0.86, respectively. The analytical model successfully reproduced the general behavior of the measured solar radiation throughout the day. A slight underprediction of direct solar radiation limited to solar noon is observed. The duration of the solar day is also captured accurately. This agreement confirms that the empirical radiation model, when combined with long-term datasets, can provide reliable estimates of the direct solar radiation for calculating the thermal performance. The error metrics are also shown in tabulated form in Table 3 and in Figure 10 for the 1st, 11th and 21st day of each month.

Although the data could be analyzed on an hourly basis, as discussed earlier, it is more informative to examine the monthly and annual performance of the system, which also highlights the local weather phenomena.

Table 3. Error metrics of DSR for summer and winter solstices and $G_{b,max}$.

	RMSE (W/m^2)	MAPE (%)	R^2
Figure 9—21 December	45	8	0.86
Figure 9—21 June	37	7	0.96
Annual Average	51	9	0.87
Figure 11	47	5	0.6

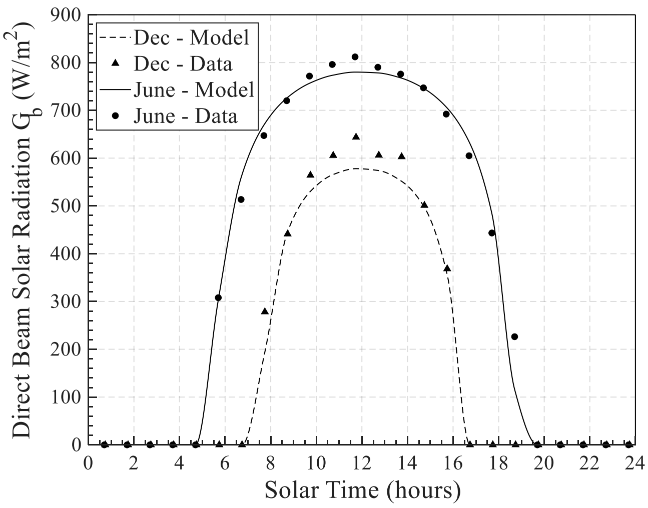

Figure 9. DSR throughout the day on 21 December (winter solstice) and 21 June (summer solstice).

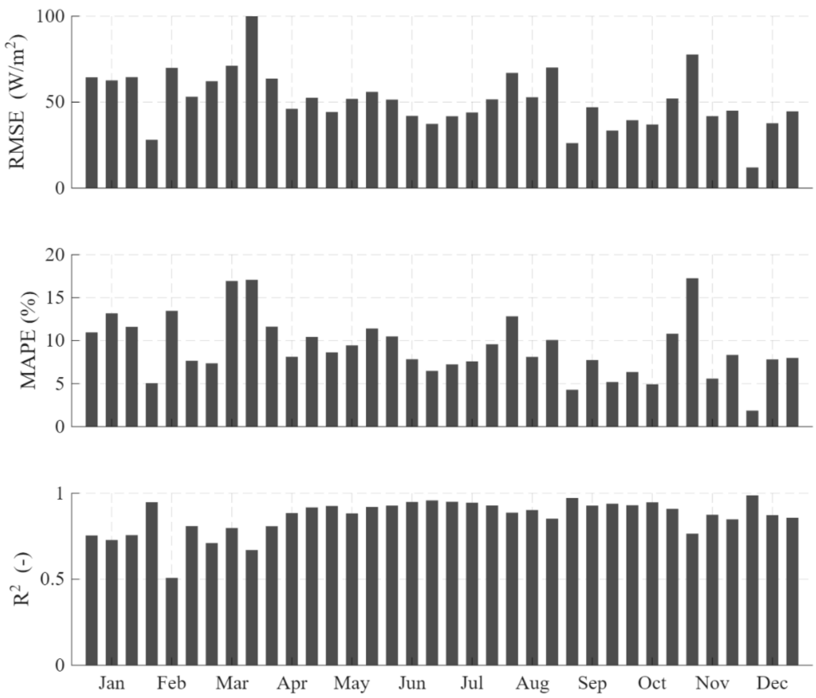

Figure 10. Monthly error metrics for the predicted DSR compared to PVGIS data for the 1st, 11th and 21st day of each month.

To further evaluate the long-term performance of the system, the maximum G_b values derived from PVGIS for the 1st, 11th and 21st day of each month were extracted, averaged and plotted in Figure 11, represented by closed circles. On the other hand, the predicted values from Equation (16) are shown with a smooth continuous line. As expected, the highest radiation levels occur during the summer months due to the increased solar altitude and longer daylight hours. Interestingly, the peak DSR is predicted to occur around early August rather than the summer solstice, highlighting the influence of local atmospheric conditions, such as humidity, aerosol concentration, and cloud cover. This observation demonstrates that solar radiation availability does not depend solely on solar geometry but is also affected by regional climatic phenomena. The error metrics are also reported in Table 3, with an overall RMSE of 47 W/m^2 and MAPE of 5%, confirming good agreement between the data.

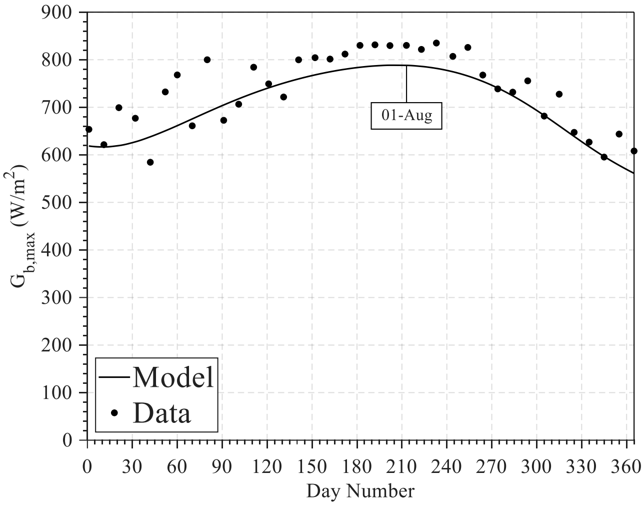

Figure 11. Maximum daily direct solar radiation G_b plotted against the day number.

3.2. Optical Performance—Incident Angle Modifier

The optical efficiency of the LFR system is strongly influenced by the incident angle modifier, which accounts for the reduction in optical performance as the solar incidence angle deviates from normal conditions. The daily variation of the maximum incident angle modifier, K_{max}, is illustrated in Figure 12. Equation (3) is first employed to calculate the instantaneous IAM, K, throughout the day, accounting for the continuous shift of the solar position. From the calculated values, the peak daily value is extracted, and K_{max} is derived. As expected, the absolute peak of K_{max} occurs during the summer solstice (21 June), with a value of 0.98, and the minimum at the winter solstice (21 December), with a value of 0.54.

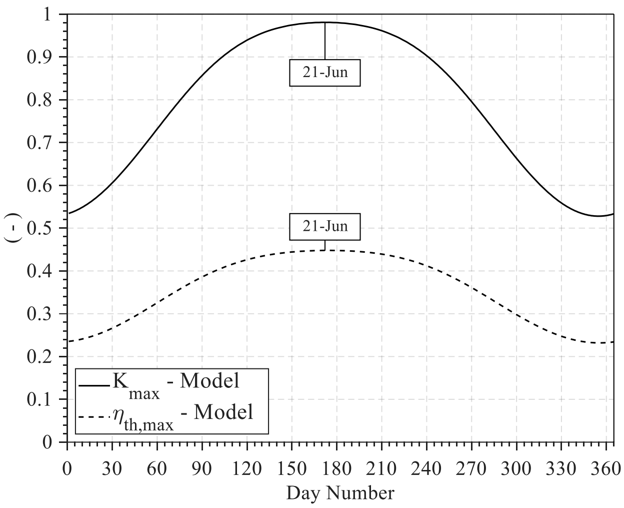

Figure 12. Maximum predicted daily IAM (K) and thermal efficiency $n_{th,max}$ with respect to the day of year.

Figure 12 also presents the annual variation of the thermal efficiency. As indicated by Equation (21), the thermal efficiency of the collector is determined by several factors, including the optical efficiency, the temperature difference between the working fluid and ambient temperature, and the available solar radiation. Among these factors, the IAM exhibits the largest influence, showing that the thermal efficiency follows a seasonal trend similar to that of K. Higher efficiencies are achieved during the summer months due to increased solar radiation levels and more favorable optical conditions.

3.3. Thermal Performance Results

The useful heat represents the actual thermal energy delivered to the working fluid and is, therefore, a key performance indicator of the system. $\dot{Q}_u$ is calculated using Equation (20), which includes the model-derived values of G_b and η_{th}. Because the thermal efficiency and the DSR reach their maximum values on different days, their product, and therefore the useful heat, peaks on an intermediate date. As shown in Figure 13, the maximum $\dot{Q}_u$ is achieved on 18 July (N = 198), delivering up to 338 W m^{-2} to the working fluid.

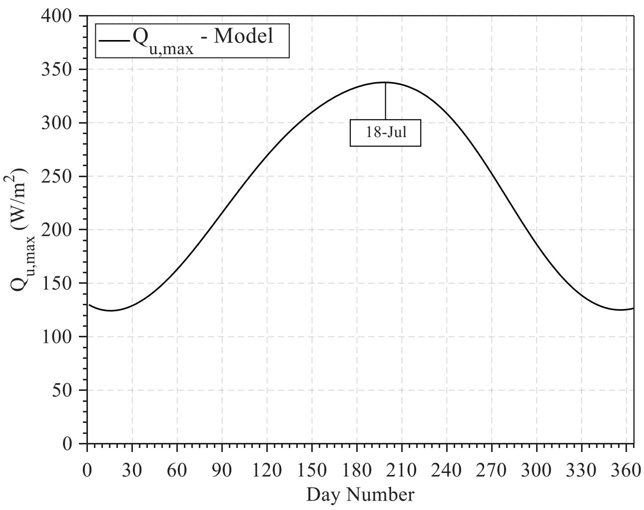

Figure 13. Variation of the predicted maximum useful heat of the LFR.

Using the coefficients A and B shown in Figure 7 in a similar manner over a period of time, the total solar energy and useful energy can be calculated using Equations (23) and (24). The quantities shown in Figures 12 and 13 are purely model-derived and could not be validated directly against experimental measurements because the corresponding data were not available. However, Montenon et al. [31] reported monthly energy outputs that will be compared against the predictions of the model.

A further validation of the proposed modeling approach is performed by comparing the predicted monthly solar and useful energy with experimental data obtained from the LFR installation at the Cyprus Institute. Figure 14 illustrates the monthly histogram of average daily energy per unit area (kWh/m^2-day), as was presented by Montenon et al. [31]. With black is shown the solar energy, and blue shows the useful energy. The narrow solid filled bars represent the reported measured values from The CyI [31], while the wide and transparent bars are the model-predicted values. The measured solar data from The CyI were collected by an on-site pyrheliometer and averaged over a period of 4 years, while the useful energy was measured directly from the system apparatus. On the other hand, the predicted data were derived from the model of this work.

There is a very good agreement between the data. The solar energy falls within the same magnitude between the measured and predicted values, with the predicted solar energy slightly overestimated for the whole year except for July. This demonstrates an encouraging trend, indicating that using open access data can yield accurate results. The agreement between model predictions and four years of pyrheliometer data demonstrates that the analytical framework can reliably replace computationally intensive ray tracing for early-stage design.

Similarly, the useful energy E_u, which was calculated from the model, yields similar values compared to the measured thermal performance of the system. Interestingly, there is a small but noticeable difference during the summer months, starting from May until

August, where the model underestimates the energy output. This is, however, not attributed to the calculation of the IAM because, as shown in Figure 5, the IAM is actually slightly overestimated by the model. Therefore, the error lies within empirical Equation (21) of the thermal efficiency of the system, which was provided by the manufacturer. Specifically, the terms include (i) the temperature difference between the inlet temperature of the fluid and the ambient temperature, which during steady state conditions is not expected to vary significantly; (ii) the predicted DSR which was shown in Figure 9 closely match to the measured values especially during the summer months, as shown by the error metrics in Figure 10; (iii) the IAM which is overestimated by the model; (iv) and the empirical coefficients of efficiency. These coefficients (namely 0.464, –0.0657 and –0.0002) are the only parameters that can increase the useful energy, and therefore, more representative values should be used.

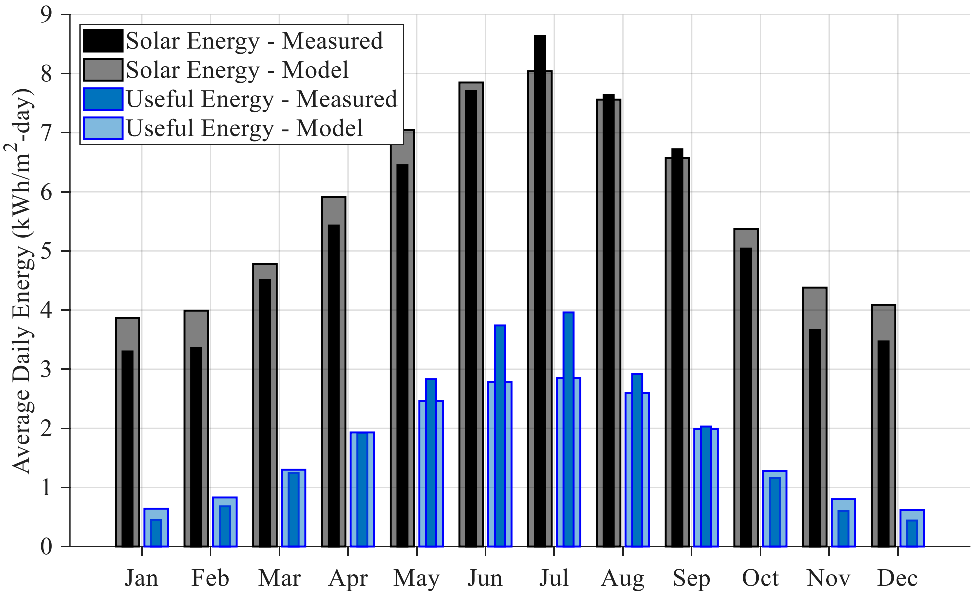

Figure 14. Histogram of solar and useful energy per day. Filled bars represent measured values from the CyI [31] and transparent bars from the model.

Further evidence for the inadequacy of the manufacturer-provided coefficients is provided by examining the theoretical upper bound of Equation (21). Setting $K = 1$ and $\Delta T/G_b = 0$ corresponds to ideal optical conditions and negligible thermal losses. Here, the maximum achievable thermal efficiency is equal to the leading coefficient, 0.464 or 46.4%. However, the maximum measured monthly thermal efficiency in Table 4 reaches 49%, which exceeds this theoretical upper limit. This internal inconsistency confirms that the manufacturer-provided coefficients underestimate the optical efficiency of the CyI system. Specifically, since the leading coefficient 0.464 effectively caps the maximum achievable efficiency in Equation (21), the model is structurally unable to reproduce the full thermal potential of the system during summer months, when solar irradiance and IAM are at their highest. This structural ceiling is, therefore, the fundamental reason for the systematic underestimation of useful energy during the summer period.

The largest discrepancy between the two methods was observed in July. The measured and estimated solar energy were 8.64 and 8.04 kWh/m^2-day, respectively, resulting in a 7% difference, while for the LFR, the measured and estimated useful energy were 3.96 and 2.85 kWh/m^2-day, respectively, resulting in a 28% difference. Overall, the results demonstrate that the proposed analytical method can successfully reproduce the optical and thermal performance of an operational LFR system using only simplified modeling approaches and open-access meteorological data.

Table 4. Measured and predicted monthly energy utilization of solar energy and averaged IAM $\overline{K}$.

Month	Solar Energy (kWh m^{-2})			LFR—Useful Energy (kWh m^{-2})			Thermal Efficiency—η_{th} (%)			$\overline{K}$ (%)
	Measured	Predicted	Diff (%)	Measured	Predicted	Diff (%)	Measured	Predicted	Diff (%)	Predicted
Jan	102	120	−17	14	20	−42	14	17	−21	39
Feb	94	112	−19	19	23	−22	20	21	−3	49
Mar	140	148	−6	38	40	−5	27	27	1	62
Apr	163	177	−9	58	58	−1	35	33	8	73
May	200	219	−9	88	76	13	44	35	20	77
Jun	231	236	−2	112	83	26	49	35	27	78
Jul	268	249	7	123	88	28	46	35	23	78
Aug	237	235	1	91	81	11	38	34	10	76
Sep	202	197	2	61	60	2	30	30	0	67
Oct	156	166	−7	36	40	−10	23	24	−4	54
Nov	110	131	−20	18	24	−33	16	18	−11	42
Dec	108	127	−18	14	19	−41	13	15	−20	36
Annual	2010	2117	−5	671	612	8%	30	27	10%	61

The measured and predicted monthly data are also presented cumulatively in Table 4 in the form of energy per m^2. That way, the monthly thermal efficiency can be calculated. For the month of July, the model-derived solar energy is 249 kWh m^{-2}, but only 88 kWh m^{-2} can be utilized, resulting in a mean thermal efficiency of 35%. For the same month, the measured data reported a thermal efficiency of 46%. The same analysis is extended for each month of the year. Finally, the total annual values are presented at the bottom of Table 4. The predicted and measured annual mean thermal efficiencies are 27% and 30%, respectively. The annual IAM is estimated by the model at 61%. As expected, the mean values of $\overline{K}$ for each month are lower compared to the maximum values presented in Figure 12.

Although the quantities $\dot{Q}_{u,max}$ and $\eta_{th,max}$ shown in Figures 12 and 13 are not directly validated against experimental data, they are derived as the product of the model-predicted G_b, which was shown to be accurately reproduced in Figure 9, and the manufacturer-supplied thermal efficiency coefficients shown in Equation (21). Additionally, the monthly solar and absorbed energy outputs shown in Figure 14 and Table 4 provide an indirect check on the combined model performance, demonstrating that the model is capable of providing reliable early-stage performance estimates, which is the primary objective of this work.

4. Conclusions

This study presented a simplified analytical method for predicting the optical and thermal performance of Linear Fresnel Reflector (LFR) systems using only geometric parameters and long-term open-access meteorological data. By using solar data from PVGIS as the basis for the ASHRAE radiation model, the direct solar radiation can be estimated at any time without requiring pyrheliometer measurements. Combined with established geometric and thermal correlations, the model successfully reproduced the annual behaviour of the LFR installed at The Cyprus Institute in Nicosia, Cyprus.

Overall, the main advantage of the proposed method is that it requires only the basic geometric characteristics of the system and is capable of producing the full annual performance within seconds with limited computational power. Therefore, compared to ray-tracing or CFD-based approaches, which require the exact geometry, specialized software, and significant setup time, the present method is considerably faster, allowing for easy parametric studies, for example, varying mirror spacing or aperture width within a very short timeframe, while the validation against four years of experimental data from the

CyI installation demonstrates that the method is sufficiently accurate for early-stage design purposes. Regarding computational cost, the difference is substantial, as a single ray-tracing or CFD simulation can take hours to days depending on the complexity of the model and the required outputs, while the present analysis produces the annual performance instantly.

The main findings are summarized below:

1. The IAM, K, exhibited a clear seasonal variation, with its maximum value consistently occurring at solar noon and peak optical performance on the summer solstice (21 June). Annual maximum values ranged between 0.54 and 0.98 depending on the day of the year;
2. The DSR was estimated using open access weather data from PVGIS [32] for over 19 years for the city of Nicosia, Cyprus. The model reproduced the DSR well both in quantity and quality. Interestingly, the maximum DSR occurred on 1 August, more than a month after the summer solstice, highlighting the influence of local atmospheric conditions;
3. The predicted thermal efficiency reached its peak during the summer solstice, consistent with the seasonal variation of the IAM and DSR. A discrepancy between the estimated and measured thermal efficiency was, however, observed during the summer months, with the largest difference occurring in July at 28%. This was attributed to the empirical coefficients of the manufacturer-provided efficiency correlation of Equation (21), rather than to the optical or radiation sub-models, which were shown to perform well independently. Further evidence of the inadequacy of these coefficients is provided by the theoretical upper bound of Equation (21), where the maximum measured monthly thermal efficiency of 49% in June exceeds the theoretical maximum of 46.4%;
4. The useful heat per unit area $\dot{Q}_u$ was calculated and presented in Figure 13 as the product of efficiency and DSR. Peak performance occurred on 18 July with values as high as 340 W m^{-2}, reflecting the combined effects of high DSR and favorable optical conditions;
5. The monthly solar E_s and useful energy E_u performance was estimated and compared to measured data directly from the system. The results showed strong agreement. However, during the summer months, the predicted useful energy was underestimated, attributed primarily to limitations in the manufacturer-provided thermal efficiency correlation rather than IAM or DSR estimation. However, the model capped the maximum achievable thermal efficiency below the levels observed in measurements, preventing the model from capturing the full thermal potential of the system and resulting in the systematic underprediction during the summer;
6. The measured and predicted annual thermal efficiency was 30% and 27%, respectively, while the mean annual predicted IAM was estimated at 61%.

The strengths of this model are closely tied to its limitations. First, it relies on a clear-sky radiation model, which may not be adequate for regions with significant cloud cover, such as locations further north than the Eastern Mediterranean. This is an interesting observation that might lead to future work. Second, the uniform mirror spacing assumption may not be representative of all LFR installations. However, the results demonstrated that, even with this simplification, the predictions were adequate for the CyI system. Third, the thermal efficiency coefficients must be supplied by the manufacturer, as they account for system-specific parameters such as the operating temperature range and working fluid. These coefficients are, therefore, not universally transferable. Fourth, the model does not account for transient effects such as thermal inertia and start-up losses, which may be relevant for operational scheduling or control system design. Researchers applying this methodology to different systems should ensure that the efficiency correlation is derived under operating conditions representative of the original system used by the designer, including the working fluid type, flow rate, and temperatures.

However, incorporating all of these effects would increase the complexity of the model and move it away from its original purpose as a rapid and accessible preliminary design tool. Future work can include the following:

1. Repeat the analysis for systems installed in more cloud-dominated locations;
2. Conduct sensitivity analyses on more geometric parameters such as mirror tilting, focal length and thermal inertia;
3. Account for the secondary reflector losses, non-uniform mirror spacing effects, and diffuse radiation contribution in the model;
4. Extend the radiation model to account for non-clear-sky conditions.

Author Contributions: Conceptualization, D.G., L.A., S.T. and P.C.; methodology, D.G., L.A. and G.C.; writing—original draft preparation, D.G., L.A. and P.C.; writing—review and editing, D.G., L.A., G.C., S.T., T.O. and P.C.; supervision, T.O. and P.C.; project administration, T.O. All authors have read and agreed to the published version of the manuscript.

Funding: This research was funded by CETPartnership, the European Partnership under Joint Call 2022 for research proposals, co-funded by the European Commission (GA N∘101069750) and with the funding organizations listed on the CETPartnership website; see Research and Innovation Foundation of Cyprus under Grant agreement EP/CETP/0922/0055.

Data Availability Statement: No new data were created or analyzed in this study. Data sharing is not applicable to this article.

Conflicts of Interest: The authors declare no competing interests.

Abbreviations

The following abbreviations are used in this manuscript:

ASHRAE	American Society of Heating, Refrigerating and Air-Conditioning Engineers
AST	Apparent Solar Time
CFD	Computational Fluid Dynamics
CSP	Concentrated Solar Power
CyI	Cyprus Institute
DSR	Direct Solar Radiation
IAM	Incident Angle Modifier
LFR	Linear Fresnel Reflector
PTC	Parabolic Trough Collector
PVGIS	Photovoltaic Geographical Information System
SARAH3	Surface Solar Radiation Dataset—Heliosat
A	Apparent Solar Radiation at Zero Air Mass
A_a	Aperture Area
B	Atmospheric Extinction Coefficient
C_p	Specific Heat Capacity
DR	Daily Temperature Variation
D_w	Distance Between Reflectors
E_s	Solar Energy
E_u	Useful Energy
F	Focal Distance
F_i	Distance Of Each Mirror from The Absorber
G_b	Direct Solar Radiation
h	Hour Angle
K	Incident Angle Modifier
$\overline{K}$	Mean Incident Angle Modifier

K_L	Incident Angle Modifier in The Longitudinal Direction
K_T	Incident Angle Modifier in The Transversal Direction
L	Local Latitude
L_c	Length Of the Collector
$\dot{m}$	Mass Flow Rate
T_{am}	Ambient Temperature
$T_{am,m}$	Mean Ambient Temperature
T_i	Inlet Fluid Temperature in the LFR
T_{out}	Outlet Fluid Temperature in the LFR
W	Distance Between the Center of the First and Last Mirror
W_0	Mirror Width
z	Solar Azimuth Angle
α	Absorbance of the Absorber
α	Solar Altitude
γ	Intercept Factor
δ	Solar Declination Angle
η_{opt}	Optical Efficiency
$\eta_{opt,max}$	Maximum Optical Efficiency
η_{th}	Thermal Efficiency
θ	Solar Incident Angle
θ_L	Longitudinal Solar Incident Angle
θ_T	Transversal Solar Incident Angle
$\theta_{T,crit}$	Critical Transversal Incident Angle
ρ	Reflectance of the Reflector
τ	Transmittance of the Cover
Φ	Solar Zenith Angle
φ_m	Mean Position Angle of the Mirror
$\dot{Q}_s$	Incident Solar Radiation
$\dot{Q}_u$	Useful Heat

Appendix A

Appendix A.1. Sensitivity Analysis on the Uniform Mirror Spacing Parameter Dw

A sensitivity analysis was performed on the mirror spacing parameter D_w to quantify its effect on the IAM predictions and to identify the dominant sources of geometric error. The baseline value of D_w = 0.433 m corresponds to the average uniform mirror spacing of the LFR system under consideration. For that reason, D_w was systematically reduced in equal steps down to the physical lower limit imposed by the mirror width W_0, below which the critical angle θ_{crit} in Equation (7) becomes undefined, and increased in increments of 10% up to double the baseline value $D_{w,max}$ = 0.866 m. Throughout the analysis, uniform mirror spacing was maintained, as introducing variable spacing per row would require fundamental modifications to the analytical equations of Bellos and Tzivanidis [24]. In total, 21 cases were evaluated, and the error metrics for each case were calculated for $\theta \leq 70°$, consistent with the approach adopted in Section 3.2.

The IAM curves for all cases are shown in Figure A1, with the corresponding error metrics plotted in Figure A2. Two distinct observations can be made.

First, decreasing D_w below the baseline consistently improves agreement with the measured CyI data across all metrics. The best case (D_w = 0.320 m, −26% from baseline) yields an RMSE of 0.027, a MAPE of 10%, and an R^2 of 0.993, compared to an RMSE of 0.051, a MAPE of 23%, and an R^2 of 0.975 for the baseline.

Second, increasing D_w beyond the baseline worsens the predictions. For values exceeding +50% of the baseline ($D_w \geq 0.65$ m), all metrics plateau, as shown in Figure A2.

This indicates that θ_{crit} is no longer triggered within the operational angular range, and any further increase of the D_w has no additional effect on the predicted K.

Importantly, at low incidence angles ($\theta < 30°$), all curves in Figure A1 converge regardless of D_w, suggesting that mirror curvature is a source of error in this regime. The two geometric simplifications, therefore, contribute to the IAM overestimation through distinct and separable mechanisms: non-uniform spacing dominates at high angles and mirror curvature dominates at low angles.

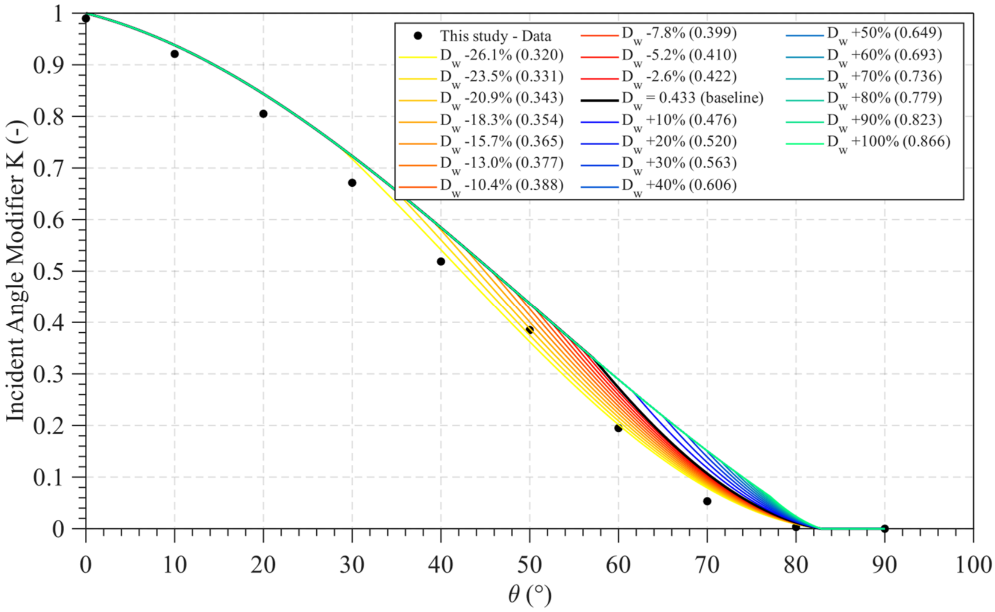

Figure A1. Sensitivity of the predicted incident angle modifier K to variations in the mirror spacing parameter D_w. The baseline case (D_w = 0.433 m) is shown in black. Values in parentheses in the legend indicate the corresponding D_w.

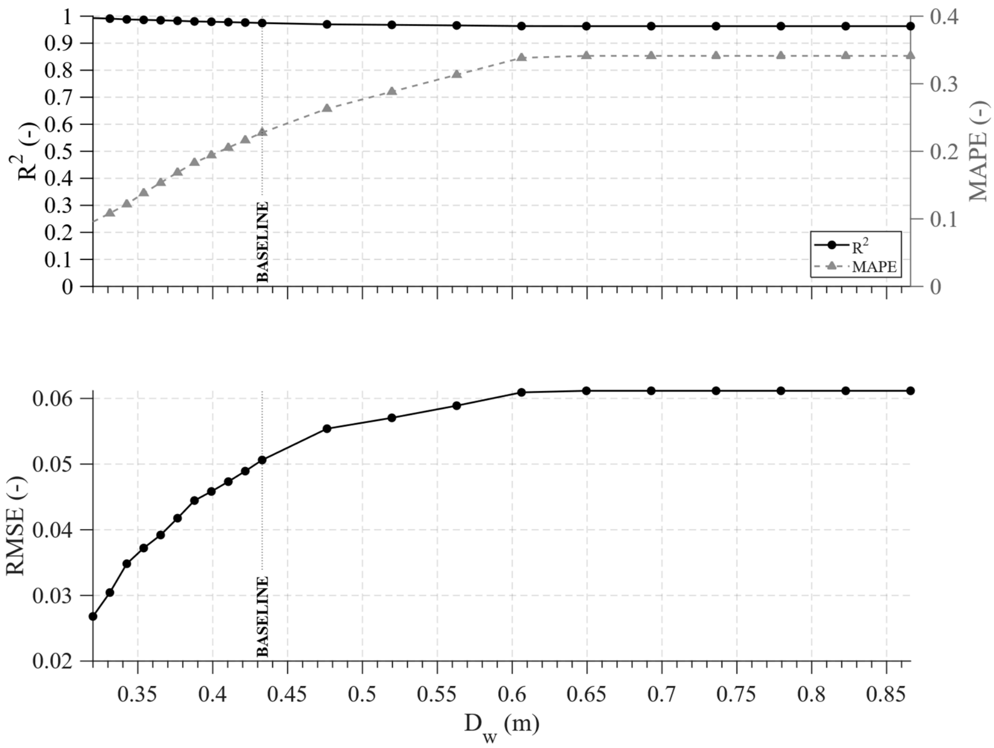

Figure A2. Error metrics for the D_w sensitivity analysis. Top plot: R^2 and MAPE, bottom plot: RMSE; all calculated for $\theta \leq 70$. Errors plateau after D_w = 0.65 m.

https://doi.org/10.3390/en19153686

Appendix A.2. Sensitivity Analysis—PVGIS Dataset

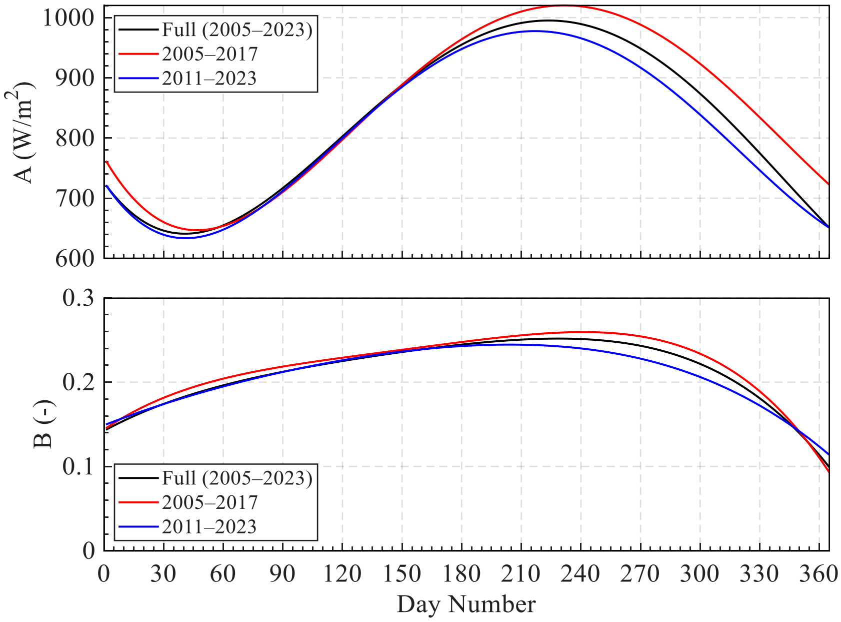

Figure A3. Sensitivity analysis of *A* and *B* parameters derived from the full 19-year PVGIS dataset (2005–2023) and two overlapping 13-year sub-periods (2005–2017 and 2011–2023) for Nicosia, Cyprus.

Table A1. Maximum deviation of A and B, compared to the full time period.

Parameter	Period	Deviation (%)
A	2005–2017	11
	2011–2023	4
B	2005–2017	6
	2011–2023	15

References

1. Kalogirou, S.A. *Solar Energy Engineering*, 1st ed.; Elsevier Science: Amsterdam, The Netherlands, 2009; ISBN 9780080922874.
2. Stein, W.H.; Buck, R. Advanced Power Cycles for Concentrated Solar Power. *Sol. Energy* **2017**, *152*, 91–105. [CrossRef]
3. IEA. *Technology Roadmap—Concentrating Solar Power*; IEA: Paris, France, 2010.
4. Caraballo, A.; Galán-Casado, S.; Caballero, Á.; Serena, S. Molten Salts for Sensible Thermal Energy Storage: A Review and an Energy Performance Analysis. *Energies* **2021**, *14*, 1197. [CrossRef]
5. Chen, H.; Cong, T.N.; Yang, W.; Tan, C.; Li, Y.; Ding, Y. Progress in Electrical Energy Storage System: A Critical Review. *Prog. Nat. Sci.* **2009**, *19*, 291–312. [CrossRef]
6. Rezk, H.; Mukhametzyanov, I.Z.; Abdelkareem, M.A.; Salameh, T.; Sayed, E.T.; Maghrabie, H.M.; Radwan, A.; Wilberforce, T.; Elsaid, K.; Olabi, A.G. Multi-Criteria Decision Making for Different Concentrated Solar Thermal Power Technologies. *Sustain. Energy Technol. Assess.* **2022**, *52*, 102118. [CrossRef]
7. Zhang, H.L.; Baeyens, J.; Degrève, J.; Cacères, G. Concentrated Solar Power Plants: Review and Design Methodology. *Renew. Sustain. Energy Rev.* **2013**, *22*, 466–481. [CrossRef]
8. Islam, M.T.; Huda, N.; Abdullah, A.B.; Saidur, R. A Comprehensive Review of State-of-the-Art Concentrating Solar Power (CSP) Technologies: Current Status and Research Trends. *Renew. Sustain. Energy Rev.* **2018**, *91*, 987–1018. [CrossRef]
9. Kuravi, S.; Trahan, J.; Goswami, D.Y.; Rahman, M.M.; Stefanakos, E.K. Thermal Energy Storage Technologies and Systems for Concentrating Solar Power Plants. *Prog. Energy Combust. Sci.* **2013**, *39*, 285–319. [CrossRef]
10. Pulido-Iparraguirre, D.; Valenzuela, L.; Fernández-Reche, J.; Galindo, J.; Rodríguez, J. Design, Manufacturing and Characterization of Linear Fresnel Reflector's Facets. *Energies* **2019**, *12*, 2795. [CrossRef]
11. Aljudaya, A.; Michailos, S.; Ingham, D.B.; Hughes, K.J.; Ma, L.; Pourkashanian, M. Techno-Economic Assessment of Molten Salt-Based Concentrated Solar Power: Case Study of Linear Fresnel Reflector with a Fossil Fuel Backup under Saudi Arabia's Climate Conditions. *Energies* **2024**, *17*, 2719. [CrossRef]

12. Mahmood, H.; Hossin, K. Daily, Monthly and Annual Thermal Performance of a Linear Fresnel Reflector to Drive an Organic Rankine-Cycle System. *Clean Energy* **2021**, *5*, 673–689. [CrossRef]
13. Arias, I.; Cardemil, J.; Zarza, E.; Valenzuela, L.; Escobar, R. Latest Developments, Assessments and Research Trends for next Generation of Concentrated Solar Power Plants Using Liquid Heat Transfer Fluids. *Renew. Sustain. Energy Rev.* **2022**, *168*, 112844. [CrossRef]
14. Ibrahim, A.; Peng, H.; Riaz, A.; Abdul Basit, M.; Rashid, U.; Basit, A. Molten Salts in the Light of Corrosion Mitigation Strategies and Embedded with Nanoparticles to Enhance the Thermophysical Properties for CSP Plants. *Sol. Energy Mater. Sol. Cells* **2021**, *219*, 110768. [CrossRef]
15. Kong, L.; Niu, Y.; Fan, D.; Shi, M.; Zheng, Z. Numerical Simulation Analysis of the Temperature Field of Molten Salt Linear Fresnel Collector. *Energies* **2025**, *18*, 5815. [CrossRef]
16. Schenk, H.; Hirsch, T.; Feldhoff, J.F.; Wittmann, M. Energetic Comparison of Linear Fresnel and Parabolic Trough Collector Systems. In Proceedings of the ASME 2012 6th International Conference on Energy Sustainability, Parts A and B, San Diego, CA, USA, 23–26 July 2012; pp. 333–344.
17. Bellos, E.; Tzivanidis, C. Assessment of Linear Solar Concentrating Technologies for Greek Climate. *Energy Convers. Manag.* **2018**, *171*, 1502–1513. [CrossRef]
18. López-Núñez, O.A.; Alfaro-Ayala, J.A.; Jaramillo, O.A.; Ramírez-Minguela, J.J.; Castro, J.C.; Damian-Ascencio, C.E.; Cano-Andrade, S. A Numerical Analysis of the Energy and Entropy Generation Rate in a Linear Fresnel Reflector Using Computational Fluid Dynamics. *Renew. Energy* **2020**, *146*, 1083–1100. [CrossRef]
19. López-Núñez, O.A.; Alfaro-Ayala, J.A.; Ramírez-Minguela, J.J.; Belman-Flores, J.M.; Jaramillo, O.A. Optimization of a Linear Fresnel Reflector Applying Computational Fluid Dynamics, Entropy Generation Rate and Evolutionary Programming. *Renew. Energy* **2020**, *152*, 698–712. [CrossRef]
20. Çalık, K.; Fırat, C. A Cost-Effective Theoretical Novel Configuration of Concentrated Photovoltaic System with Linear Fresnel Reflectors. *J. Polytech.* **2019**, *22*, 583–589. [CrossRef]
21. Wang, G.; Wang, F.; Shen, F.; Jiang, T.; Chen, Z.; Hu, P. Experimental and Optical Performances of a Solar CPV Device Using a Linear Fresnel Reflector Concentrator. *Renew. Energy* **2020**, *146*, 2351–2361. [CrossRef]
22. Machado da Costa, A.F.; Marques Lameirinhas, R.A.; Pinho Correia Valério Bernardo, C.; Neto Torres, J.P.; Santos, M. The Modeling of Concentrators for Solar Photovoltaic Systems. *Energies* **2024**, *17*, 3201. [CrossRef]
23. Rungasamy, A.E.; Craig, K.J.; Meyer, J.P. A Review of Linear Fresnel Primary Optical Design Methodologies. *Sol. Energy* **2021**, *224*, 833–854. [CrossRef]
24. Bellos, E.; Tzivanidis, C. Development of Analytical Expressions for the Incident Angle Modifiers of a Linear Fresnel Reflector. *Sol. Energy* **2018**, *173*, 769–779. [CrossRef]
25. Grena, R. Geometrical Aspects of the Optics of Linear Fresnel Concentrators: A Review. *Energies* **2024**, *17*, 3564. [CrossRef]
26. Sepúlveda, F.J.; Miranda, M.T.; Montero, I.; Arranz, J.I.; Lozano, F.J.; Matamoros, M.; Rodríguez, P. Analysis of Potential Use of Linear Fresnel Collector for Direct Steam Generation in Industries of the Southwest of Europe. *Energies* **2019**, *12*, 4049. [CrossRef]
27. Bellos, E.; Tzivanidis, C.; Papadopoulos, A. Daily, Monthly and Yearly Performance of a Linear Fresnel Reflector. *Sol. Energy* **2018**, *173*, 517–529. [CrossRef]
28. ASHRAE. *Handbook of Fundamentals*; American Society of Heating, Refrigerating and Air-Conditioning Engineers: Atlanta, GA, USA, 1985.
29. Boccalatte, A.; Fossa, M.; Ménézo, C. Calculation of the Incidence Angle Modifier of a Linear Fresnel Collector: The Proposed Declination and Zenith Angle Model Compared to the Biaxial Factored Approach. *Renew. Energy* **2022**, *185*, 123–138. [CrossRef]
30. Sallaberry, F.; Mutuberria Larrayoz, A. Optical Efficiency and Incidence Angle Modifier Characterization of a Linear Fresnel Reflector Collector: Validation of a Certified on-Site Test Combining Experimental Measurements and Simulation Results. *Sol. Energy* **2024**, *267*, 112142. [CrossRef]
31. Montenon, A.C.; Santos, A.V.; Collares-Pereira, M.; Montagnino, F.M.; Garofalo, R.; Papanicolas, C. Optical Performance Comparison of Two Receiver Configurations for Medium Temperature Linear Fresnel Collectors. *Sol. Energy* **2022**, *240*, 225–236. [CrossRef]
32. Photovoltaic Geographical Information System. Available online: https://re.jrc.ec.europa.eu/ (accessed on 1 March 2026).
33. McIntire, W.R. Factored Approximations for Biaxial Incident Angle Modifiers. *Sol. Energy* **1982**, *29*, 315–322. [CrossRef]
34. Montenon, A.C.; Fylaktos, N.; Montagnino, F.; Paredes, F.; Papanicolas, C.N. Concentrated Solar Power in the Built Environment. *AIP Conf. Proc.* **2017**, *1850*, 040006. [CrossRef]
35. Papanicolas, C.; Lange, M.A.; Fylaktos, N.; Montenon, A.; Kalouris, G.; Fintikakis, N.; Fintikaki, M.; Kolokotsa, D.; Tsirbas, K.; Pavlou, C.; et al. Design, Construction and Monitoring of a near-Zero Energy Laboratory Building in Cyprus. *Adv. Build. Energy Res.* **2015**, *9*, 140–150. [CrossRef]
36. Bellos, E.; Tzivanidis, C.; Papadopoulos, A. Optical and Thermal Analysis of a Linear Fresnel Reflector Operating with Thermal Oil, Molten Salt and Liquid Sodium. *Appl. Therm. Eng.* **2018**, *133*, 70–80. [CrossRef]

37. Montenon, A.C.; Papanicolas, C. Economic Assessment of a PV Hybridized Linear Fresnel Collector Supplying Air Conditioning and Electricity for Buildings. *Energies* **2021**, *14*, 131. [CrossRef]
38. CST Modelling Tools—Tonatiuhpp. Available online: https://github.com/CST-Modelling-Tools/tonatiuhpp/wiki (accessed on 15 July 2026).
39. Katiyar, A.K.; Pandey, C.K. A Review of Solar Radiation Models—Part I. *J. Renew. Energy* **2013**, *2013*, 1–11. [CrossRef]
40. El Mghouchi, Y.; El Bouardi, A.; Choulli, Z.; Ajzoul, T. Models for Obtaining the Daily Direct, Diffuse and Global Solar Radiations. *Renew. Sustain. Energy Rev.* **2016**, *56*, 87–99. [CrossRef]
41. El Mghouchi, Y.; Ajzoul, T.; Taoukil, D.; El Bouardi, A. The Most Suitable Prediction Model of the Solar Intensity, on Horizontal Plane, at Various Weather Conditions in a Specified Location in Morocco. *Renew. Sustain. Energy Rev.* **2016**, *54*, 84–98. [CrossRef]
42. Kouremenos, D.A.; Antonopoulos, K.A.; Domazakis, E.S. Solar Radiation Correlations for the Athens, Greece, Area. *Sol. Energy* **1985**, *35*, 259–269. [CrossRef]
43. Perrin de Brichambaut, C. *Estimation Des Ressources Énergétiques En France*; AFEDES: Paris, France, 1975.
44. Capderou, M. (Ed.) *Atlas Solaire de l'Algérie Énergétique*; OPU Alger: Algiers, Algeria, 1985; Volume 2.
45. Bird, R.E.; Hulstrom, R.L. *Simplified Clear Sky Model for Direct and Diffuse Insolation on Horizontal Surfaces*; Solar Energy Research Institute: Golden, CO, USA, 1981.